PHYSICAL REVIEW B **104**, 035301 (2021)

Magnetic field controllable planar Hall effect in Sr_2IrO_4 films

Mingrui Liu,[1,2] Haiwen Liu,[1] Tingna Shao,[1] Weimin Jiang,[1] Zitao Zhang,[1] Jingzhuo Ling,[1] Chunli Yao,[1] Yujie Qiao,[1]
Qiang Zhao,[1] Changmin Xiong,[1] Ruifen Dou,[1,*] and Jiacai Nie[1,†]
[1]*Department of Physics, Beijing Normal University, Beijing 100875, People's Republic of China*
[2]*State Key Laboratory of Luminescence and Applications, Changchun Institute of Optics, Fine Mechanics and Physics,*
Chinese Academy of Sciences, Changchun 130033, China

(Received 18 December 2020; revised 10 April 2021; accepted 16 June 2021; published 6 July 2021)

The planar Hall effect (PHE) has remarkable advantages for applications to spintronic devices and the study of intrinsic magnetic properties because of its high signal-to-noise ratio and low thermal drift. Here, the magnetic field controllable PHE in $Sr_2IrO_4/SrTiO_3$ (001) films is presented. The PHE transforms from a "sinusoidal-shaped" twofold symmetry to fourfold oscillations with decrease in the magnetic field at 35 K. Furthermore, the PHE is approximately two to three orders of magnitude larger than the giant PHE associated with ferromagnetic semiconductors as the temperature decreases. Based on subsequent measurements of the magnetic transport properties and calculations of the angle between the magnetization and current, the unexpected fourfold-symmetric PHE can be attributed to magnetocrystalline anisotropy and spin-orbital coupling. These observations of PHE facilitate a deeper understanding of the magnetic interactions in Sr_2IrO_4 films and indicate potential applications in spintronic or magnetic-sensor devices.

DOI: 10.1103/PhysRevB.104.035301

I. INTRODUCTION

Sensors utilizing the planar Hall effect (PHE) have attracted considerable attention for magnetoresistive devices [1–3]. PHE is different from the traditional Hall effect, wherein the orientation of the magnetic field is out of plane and perpendicular to the current; the magnetic field and current are in the same plane in PHE [4,5]. PHE can be attributed to the anisotropy in the resistivity tensor because of spin-orbit coupling (SOC). The planar Hall resistance can be given as follows:

$$R_{xy} = \frac{1}{2}(R_{//} - R_{\perp})\sin 2\phi, \qquad (1)$$

where R_{xy} is the transverse resistance, $R_{//}$ and $R_{\perp}$ are the resistances when the current is parallel and perpendicular to the magnetization, respectively, and φ is the angle between the directions of the magnetization and current [6,7]. Hong *et al.* [8] reported related phenomena in metallic ferromagnets; however, a considerably small effect can be observed in this case, usually on the order of mΩ. Subsequently, a giant PHE was reported in $La_{0.84}Sr_{0.16}MnO_3$ thin films [9] and ferromagnetic semiconductors such as (Ga,Mn)As [10] (the effect is approximately four orders of magnitude larger than that found in metallic ferromagnets). Remarkably, as a twin effect to anisotropic magnetoresistance (AMR), PHE is more sensitive to the orientation of the in-plane magnetic moment than AMR [4,5] and exhibits the advantages of high signal-to-noise ratio [11] and low thermal drift [3]. Hence, it has been applied widely in magnetic random-access memory and other nonvolatile storage devices [11–14].

Recently, Sr_2IrO_4, which is a candidate unconventional superconductor, has been extensively studied [15–18]. The 5*d* transition-metal oxide Sr_2IrO_4 has stronger SOC interactions than 3*d* compounds such as (Ga,Mn)As and $La_{0.84}Sr_{0.16}MnO_3$ because the magnitude of SOC is proportional to the fourth power of the atomic number [19]. In addition, a net magnetic moment could be observed in each IrO_2 layer, which can be attributed to the rotation of the IrO_6 octahedra about the *c* axis [20,21]. Further, the spin-flip transition can be triggered by applying a small magnetic field (0.2 T) in the *ab* plane, resulting in a weak ferromagnetic phase in Sr_2IrO_4 [22–24], as can be observed from Fig. 1(a). The fascinating magnetic properties and strong SOC interaction provide considerable motivation for studying the PHE in this system.

In this paper, magnetic field controllable PHE was observed in Sr_2IrO_4 films. At 35 K, a fourfold-symmetric oscillation in the PHE emerged with the decreasing magnetic field. Subsequent measurements indicated that this fourfold-symmetric PHE can be attributed to the magnetocrystalline anisotropy and SOC. Remarkably, the magnitude of PHE is approximately two to three orders of magnitude larger than the giant PHE in ferromagnetic semiconductors as the temperature decreases. In addition, R_{xy} shows a spin-valve-like switching behavior when the magnetic field is swept in the plane. These results are valuable for studying the magnetic interactions in this system and shed light on the potential of Sr_2IrO_4 for applications in magnetoresistive devices.

II. EXPERIMENTS

Atomically flat TiO_2-terminated (001) $SrTiO_3$ substrates were prepared via etching in a NH_4F-buffered Hydrofluoric acid solution ($pH = 5.1$). They were then annealed at 930 °C for 2 h in an oxygen atmosphere. A Sr_2IrO_4 film was then

---

[*] ruifendou@bnu.edu.cn
[†] jcnie@bnu.edu.cn

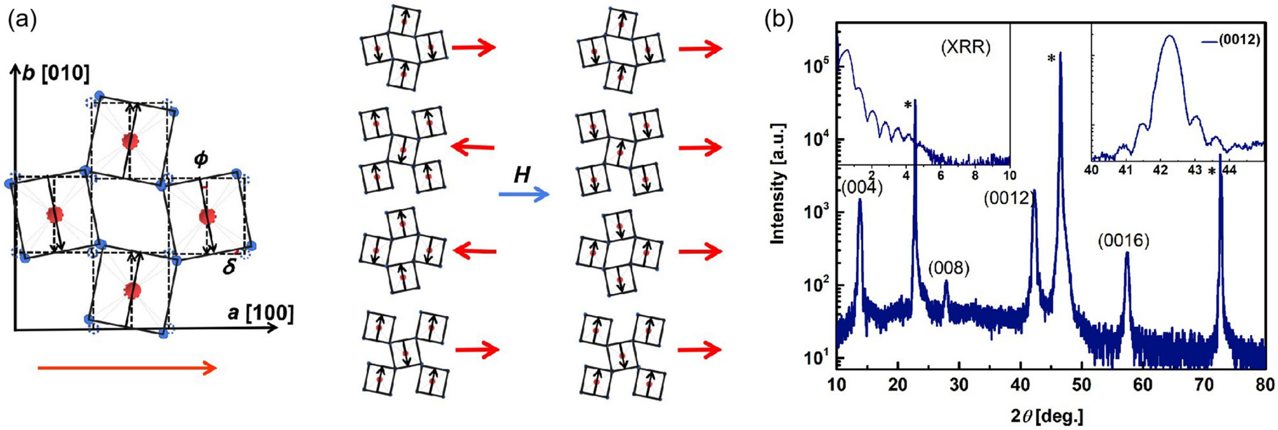

FIG. 1. (a) Mechanism for generating a net in-plane magnetic moment. The rotations of the IrO_6 octahedra and the relation between the octahedral rotation angle δ and the isospin canting angle $\phi(\delta \approx \phi)$ are presented in the left panel. The red circles denote Ir^{4+}, whereas the blue circles denote O^{2-}. The red arrow indicates the net moment. The right panel shows the antiferromagnetic structure of Sr_2IrO_4. A weak ferromagnetic phase is induced by the isospin-flip transitions when an in-plane magnetic field is applied. (b) X-ray-diffraction patterns of the $Sr_2IrO_4/SrTiO_3$ (001) thin film. The asterisks indicate the diffraction peaks of the $SrTiO_3$ substrate. The inset shows the x-ray reflectivity patterns, and the Laue oscillations around the (0012) peak, based on which the thickness of the Sr_2IrO_4 thin film can be determined [25].

grown on the annealed (001) $SrTiO_3$ substrate via pulsed laser deposition when considering the stoichiometric Sr_2IrO_4 polycrystalline pellet as the target. The growth parameters have been discussed previously [25].

We characterized the epitaxial structures and thicknesses of the films based on their x-ray-diffraction patterns (x-ray diffractometer: Cu K-α1 radiation of wavelength $\lambda = 0.154\ 06$ nm). Further, we measured the temperature- and magnetic-field dependence of the magnetic transport properties using a conventional four-probe configuration based on a Physical Properties Measurement System (Quantum Design) with a constant channel current I of 0.1 μA applied along the [100] direction.

III. RESULTS AND DISCUSSION

Figure 1(b) shows the x-ray-diffraction pattern of Sr_2IrO_4 film epitaxially deposited on a single-crystal (001) $SrTiO_3$ substrate. The left inset of Fig. 1(b) is the x-ray reflectivity patterns; the right inset shows the significant Laue fringe peaks around the (0012) peak, indicating good epitaxial characteristics. The film thickness determined from the adjacent reflectivity peaks was 12.51 nm, and that calculated from the satellite peaks was 13.82 nm. Hence, we take the average thickness as 13.17 nm.

We initially studied the PHE in the Sr_2IrO_4 film with a constant in-plane magnetic field ($H = 9$T) at different temperatures. To exclude the contribution of the longitudinal resistance R_{xx} owing to a slight misalignment of the electrodes, we normalized all the R_{xy} measurements in this paper as [26]

$$R_{xy} = R_{xy}^{\mathrm{raw}} - R_{xx} \cdot \frac{R_{xy}^{\mathrm{raw}}(0)}{R_{xx}(0)}. \tag{2}$$

Here, $R(0)$ denotes R_{xy} and R_{xx} at 0 T. Figure 2(a) presents R_{PHE} as a function of θ, where $R_{\mathrm{PHE}} = R_{xy}(\theta) - R_{xy}(0^\circ)$ and θ is the angle between H and I. The measurement setup is schematically presented in Fig. 2(b). At 150 and 100 K, the PHE exhibits a sinusoidal-shaped twofold symmetry with four extremes at $\theta = 45^\circ$, 135°, 225°, and 315°, which can be fitted well using Eq. (1). As the temperature decreases, the PHE signal increases rapidly; however, the shape of the PHE is distorted at the same time. At 35 K, the peaks at 135° and 315° gradually sink into troughs with the decrease of H, and a fourth-order term must be added to ensure better fitting of the PHE data [27,28], which can be seen in Fig. 2(c)

Figure 3(a) presents the quantitative relation between the percentage deviation of the PHE obtained from Eq. (1) as a function of the magnetic field.

$$\Delta R_{\mathrm{PHE}-135^\circ} = \frac{R_{\mathrm{fitting}}(135^\circ) - R_{xy}(135^\circ)}{R_{xy}(135^\circ)} \times 100\%. \tag{3}$$

The degree of deviation increases as the magnetic field decreases. To further investigate the anomalous PHE, we measured the temperature dependence of R_{xy} with the magnetic field fixed at 135° in the plane. As shown in Fig. 3(b), R_{xy} increases with the decreasing temperature at different magnetic field. However, R_{xy} drastically reduces at approximately 45 K. This phenomenon does not emerge in the temperature dependence of R_{xx}; see Fig. S1 in the Supplemental Material [29] for more details. Furthermore, the smaller the magnetic field, the more will be the decrease in R_{xy}, which is consistent with that observed in previous measurements [Fig. 3(a)]. When a magnetic field is applied, the direction of the magnetic moment can be determined based on the Zeeman energy and the magnetic-anisotropy energy [30]. The former is proportional to the magnetic field [30], and the latter is dominated by the magnetocrystalline-anisotropy energy, which is related to the SOC and is more pronounced at low temperatures [24]. The magnetic-anisotropy energy dominates the Zeeman energy at low magnetic fields and temperatures, and it is preferred to align magnetization with the easy axis (see Fig. S2 in the Supplemental material [29], which includes Refs. [31,32].) instead of following the magnetic field direction [27,30,33]. Hence, the fourfold-symmetric PHE in Sr_2IrO_4 films can be

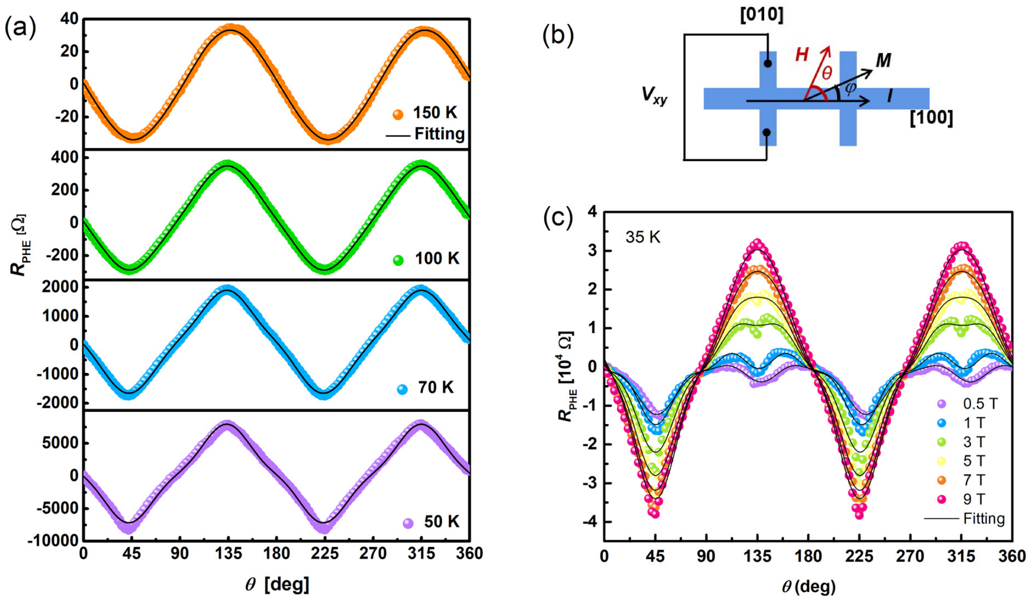

FIG. 2. (a) θ dependence of R_{PHE} at different temperatures for the Sr_2IrO_4 film at 9 T. Black lines indicate fitting to Eq. (1). (b) Schematic of the PHE measurement setup, wherein a current I is applied along the [100] direction and H is rotated in plane. Here, θ is the angle between H and I, and φ is the angle between the magnetization M and I. (c) $R_{\mathrm{PHE}}(\theta)$ for different magnetic fields at 35 K. Black lines indicate fitting to the data obtained when a fourth-order term is added in Eq. (1).

mainly attributed to the magnetocrystalline anisotropy. Thus, the troughs at $\theta = 135^\circ$ and 315° will be more obvious in smaller magnetic fields. As shown in the inset in Fig. 3(b), the PHE transforms into a fourfold symmetry at 0.2 T, which is consistent with our assertion. Below 0.2 T, the magnetic field cannot trigger spin-flip transitions [Fig. 1(a)] [22–24], making it impossible to detect the PHE and other signals associated with the properties of magnetic transport.

To further validate our assertion, we extracted the angle φ from R_{PHE} as follows [30]:

$$\phi = \tfrac{1}{2}\sin^{-1}(R_{\mathrm{PHE}}/R_{\mathrm{PHE,max}}). \qquad (4)$$

The relation between φ and θ manifests the energy competition between the Zeeman energy and the magnetic-anisotropy energy [34]. Figure 4(a) shows the $\varphi(\theta)$ extracted from $R_{\mathrm{PHE}}(\theta)$ within the quadrant $\theta = [135^\circ, 180^\circ]$ at different magnetic fields and temperatures. At 35 K, as shown by solid points, φ lags behind θ. Further, the smaller the magnetic field, the more $\varphi(\theta)$ will deviate from linearity. With increasing temperature at 9 T, the nonlinearity of $\varphi(\theta)$ gradually decreases, and an almost linear relation can be observed at 100 K (hollow points). To quantify the nonlinearity, we calculated the residual sum of squares (RSS) of the linear fit to $\varphi(\theta)$: RSS $= \sum i[\varphi(\theta i) - (\theta i)]^2$. In Fig. 4(b), RSS decreases with the increasing temperature and magnetic field. At 100 K, RSS is almost saturated beyond the anisotropy field (3 T), at which we consider the condition $\varphi \approx \theta$ to have been reached. These results further confirm that the fourfold symmetry of the PHE

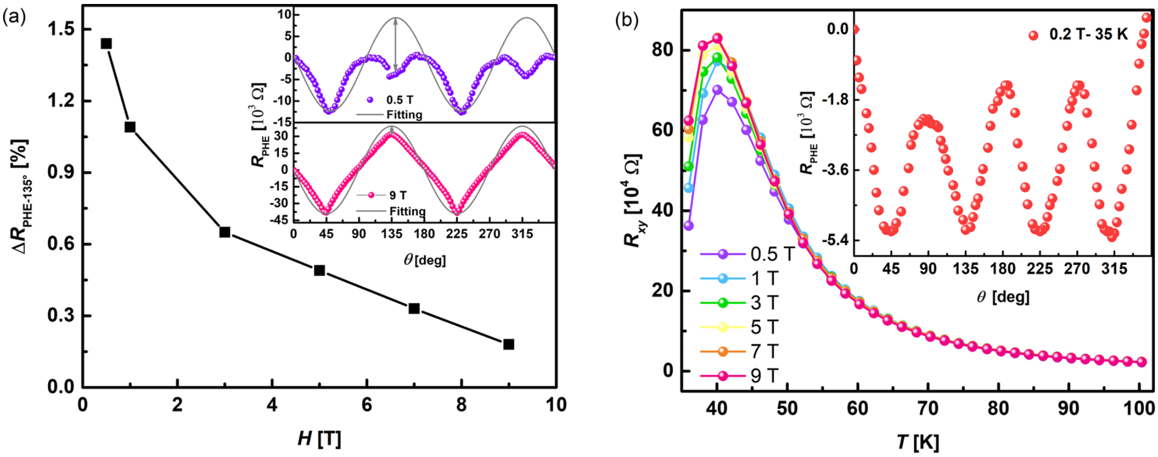

FIG. 3. (a) Percentage deviation of the PHE obtained from Eq. (1) vs the magnetic field. Inset: The double arrow represents the magnitude of the deviation obtained by considering 0.5 and 9 T as examples. (b) Temperature-dependent R_{xy} for different magnetic fields at $\theta = 135^\circ$. Inset: θ dependence of R_{PHE} at 0.2 T.

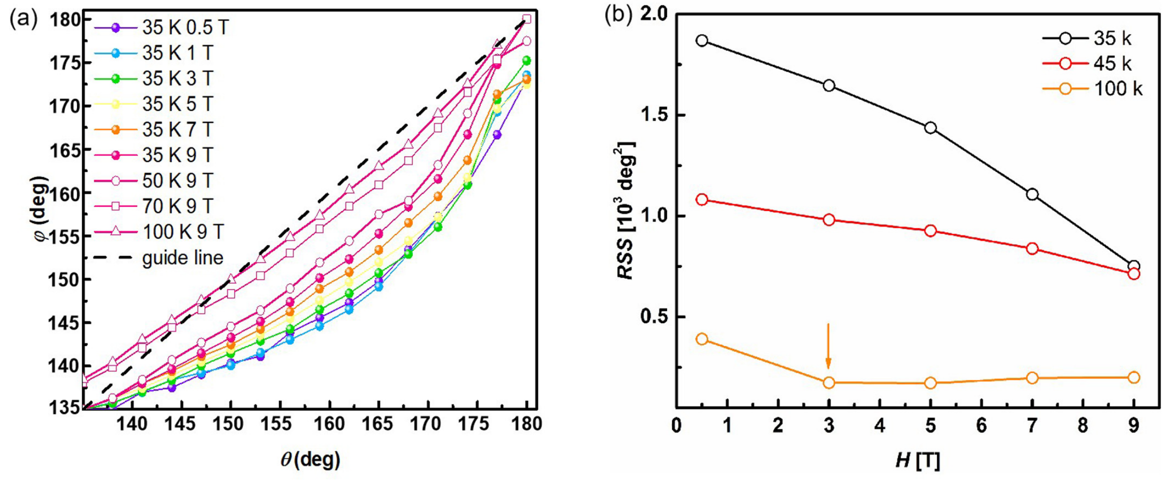

FIG. 4. (a) Extracted φ vs θ. Solid points denote $\varphi(\theta)$ at 35 K for different magnetic fields, whereas hollow points denote $\varphi(\theta)$ at 9 T for different temperatures. The black dashed line is a guide for the eyes when $\varphi \approx \theta$ (b) The RSS (see text) as a function of H at 35, 45, and 100 K. The arrow marks the corresponding anisotropy field at 100 K.

can be attributed to the competition between the Zeeman energy and the intrinsic magnetocrystalline-anisotropy energy.

We also investigated the in-plane magnetic field dependent R_{xy} at 35 K when $\theta = 20^\circ$ to obtain further information regarding PHE. The value of R_{xy} shows a switching behavior similar to that of a spin valve. As illustrated previously [22,23,29], the easy magnetization axis of Sr_2IrO_4 is along the [110] direction. The insets of Fig. 5 show the magnetization orientations relative to the easy axes (black and gray dashed lines) for different external magnetic fields. By considering the black circles in Fig. 5 as an example, the direction of magnetization exhibits sequential changes owing to variations of the applied magnetic field from maximum positive to maximum negative values. At high positive fields, magnetization is aligned close to the direction of the external magnetic field, as indicated by state *A*. As the field is reduced, magnetization gradually aligns along the easy axis (black dashed lines, state *B*), which causes R_{xy} to decrease owing to the stability of the magnetization along a particular easy-axis direction [6,35]. As the field orientation is reversed, the magnetization switches to the other easy axis (gray dashed lines, state *C*). Due to the two easy magnetization axes being perpendicular to each other [20], according to Eq. (1) in the main text, the sign of R_{xy} will reverse. Hence, R_{xy} increases as the negative fields increases. Finally, with further increasingly negative fields, magnetization gradually becomes aligned with the external magnetic field direction again (state *D*) [9,35].

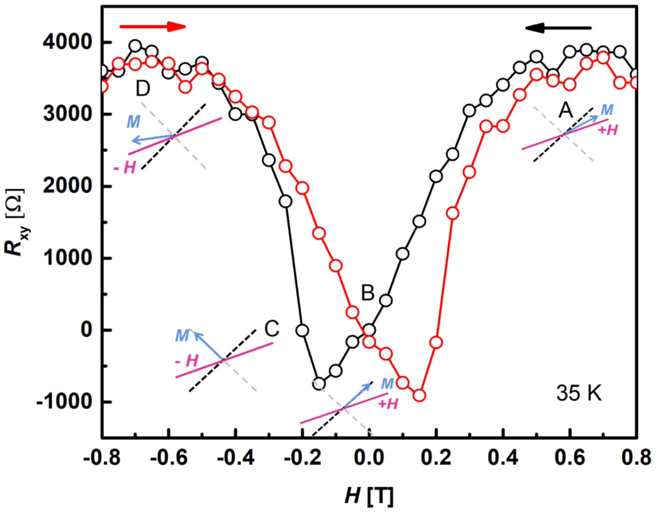

FIG. 5. In-plane magnetic field dependent R_{xy} at 35 K and $\theta = 20^\circ$. The black and red arrows indicate the sweep direction of the field. Insets show the spin configurations for the magnetic-reversal process, where the dashed lines denote the direction of the easy axis, the pink lines indicate the magnetic field direction, and the blue arrows denote the net magnetization.

In 2019, Everhardt *et al.* also mentioned PHE when they took second-harmonic Hall measurements to determine the spin Hall angle of Sr_2IrO_4/NiFe bilayer structure [36]. In their work, a low-frequency ac current flows through a Hall bar, and due to the large spin-orbit coupling in Sr_2IrO_4, the Rashba-Edelstein effect generates nonequilibrium spin accumulation near the Sr_2IrO_4/NiFe interface which can diffuse into the ferromagnet. Those spin currents exert a torque on the magnetization in the ferromagnetic material NiFe. What is measured is the transverse voltage of the entire heterojunction. And, due to the large resistivity mismatch between NiFe and Sr_2IrO_4, the first-harmonic signal $R_{1\omega}$ is the PHE dominated by NiFe. Note that the magnitude of $R_{1\omega}$ in their work is very small ($10^{-1}\,\Omega$), which is consistent with the magnitude of PHE in ferromagnetic metals reported previously [37]. However, in our work, a dc current flows along the direction of [100] of the film, and what we measure is the PHE of Sr_2IrO_4 film. Hence, the magnitude of PHE in our work is much larger than that reported by Everhardt *et al.* Furthermore, the magnitude of PHE was compared with the giant PHE in $La_{0.84}Sr_{0.16}MnO_3$ [9] under the same measurement conditions. As shown in Fig.S3 [29], at 100 K, the magnitude of PHE in Sr_2IrO_4 is $10^3(\mu\Omega\,\mathrm{cm})$, which is approximately one order of magnitude larger than $La_{0.84}Sr_{0.16}MnO_3$. For lower temperature such as 40 K, the magnitude of PHE in

Sr_2IrO_4 is $10^4 (\mu\Omega\,\mathrm{cm})$, which is approximately three orders of magnitude larger. Such large PHE is attributed to the SOC of the 5d transition-metal oxide Sr_2IrO_4 being much greater than that of the 3d compound. As a twin effect of PHE, the combination of atomic-scale giant-magnetoresistance-like effect and magnetocrystalline anisotropy energy caused by strong SOC is also reflected in the giant AMR of Sr_2IrO_4 single crystal [32]; see S4 [29] in the Supplemental Material for more details.

In addition, the growth oxygen pressure plays a very important role in the stabilization and transport properties of stoichiometric iridates [38,39]. In Fig. S5 [29], the XRD patterns verify that the film in our work is single-phase Sr_2IrO_4 when the oxygen pressure ranges from 10^{-5} to 10^{-2} mbar, and the conductivity and film flatness of Sr_2IrO_4 are improved with the increase of oxygen pressure. The resistance of samples grown below 10^{-2} mbar is out of measuring range when the temperature decreases at 45 K. Therefore, the fourfold-symmetric PHE under low temperature and small magnetic field cannot be observed, but the PHE is a sinusoidal-shaped twofold symmetry above 60 K, which can be seen in Fig. S5(d). In order to further verify the validity of the conclusions, we grow a 26-nm Sr_2IrO_4 film under 10^{-2} mbar. Due to the increase in thickness, the magnetism of the sample is enhanced, and the magnetocrystalline anisotropy is more pronounced. The PHE under different magnetic fields at 35 K is all fourfold symmetry, but the change trend is the same as that of the 13.17-nm sample in the main text (Fig. S6).

IV. CONCLUSION

In summary, PHE was first observed in a 13.17-nm-thick Sr_2IrO_4 film, and it is at least two orders of magnitude larger than the giant PHE in ferromagnetic semiconductors. As the magnetic field decreases, a fourfold PHE symmetry emerges unexpectedly at 35 K. $\varphi(\theta)$ calculations show that magnetic field controllable PHE can be mainly attributed to strong SOC and magnetocrystalline anisotropy. In addition, R_{xy} shows a spin-valve-like switching behavior when the magnetic field is swept in the plane. These observations facilitate a deeper understanding of the magnetic interactions in Sr_2IrO_4 films and their applications to magnetic sensors and nonvolatile memory devices.

ACKNOWLEDGMENTS

We thank Zengyao Ren and Xinxiang Chen for discussing the experimental data. We also thank the National Natural Science Foundation of China (Grants No. 11674031, No. 11474022, No. 11474024, No. 11422430, No. 11974048, and No. 11374035) and the National Basic Research Program of China (Grants No. 2014CB920903 and No. 2013CB921701) for their financial support.

---

[1] S. S. Parkin, C. Kaiser, A. Panchula, P. M. Rice, B. Hughes, M. Samant, and S. H. Yang, Nat. Mater. **3**, 862 (2004).
[2] S. S. P. Parkin, M. Hayashi, and L. Thomas, Science **320**, 190 (2008).
[3] B. Ozer, H. Piskin, and N. Akdogan, IEEE Sens. J. **19**, 5493 (2019).
[4] K. Okamoto, J. Magn. Mater. **35**, 353 (1983).
[5] Y. Liu, J. Yang, W. Wang, H. Du, W. Ning, L. Ling, W. Tong, Z. Qu, G. Cao, Y. Zhang, and M. Tian, Phys. Rev. B **95**, 161103(R) (2017).
[6] A. V. Kudrin, O. V. Vikhrova, and Y. A. Danilov, Tech. Phys. Lett. **36**, 511 (2010).
[7] T. R. Mcguire and R. I. Potter, IEEE Trans. Magn. **11**, 1018 (1975).
[8] K. Hong and N. Giordano, Phys. Rev. B **51**, 9855 (1995).
[9] Y. Bason, L. Klein, J. B. Yau, X. Hong, and C. H. Ahn, Appl. Phys. Lett. **84**, 2593 (2004).
[10] H. X. Tang, R. K. Kawakami, D. D. Awschalom, and M. L. Roukes, Phys. Rev. Lett. **90**, 107201 (2003).
[11] T. Q. Hung, F. Terki, S. Kamara, K. Kim, S. Charar, and C. Kim, J. Appl. Phys. **117**, 154505 (2015).
[12] L. Ejsing, M. F. Hansen, A. K. Menon, H. A. Ferreira, D. L. Graham, and P. P. Freitas, Appl. Phys. Lett. **84**, 4729 (2004).
[13] W. L. Lim, X. Liu, K. Dziatkowski, Z. Ge, S. Shen, J. K. Furdyna, and M. Dobrowolska, Phys. Rev. B **74**, 045303 (2006).
[14] Y. Bason, L. Klein, J.-B. Yau, X. Hong, J. Hoffman, and C. H. Ahn, J. Appl. Phys. **99**, 08R701 (2006).
[15] F. Wang and T. Senthil, Phys. Rev. Lett. **106**, 136402 (2011).
[16] H. Watanabe, T. Shirakawa, and S. Yunoki, Phys. Rev. Lett. **110**, 027002 (2013).
[17] B. Zwartsenberg, R. P. Day, E. Razzoli, M. Michiardi, N. Xu, M. Shi, J. D. Denlinger, G. Cao, S. Calder, K. Ueda, J. Bertinshaw, H. Takagi, B. J. Kim, I. S. Elfimov, and A. Damascelli, Nat. Phys. **16**, 290 (2020).
[18] Y. K. Kim, N. H. Sung, J. D. Denlinger, and B. J. Kim, Nat. Phys. **12**, 37 (2016).
[19] L. F. Mattheiss, Phys. Rev. B **13**, 2433 (1976).
[20] C. Dhital, T. Hogan, Z. Yamani, C. delaCruz, X. Chen, S. Khadka, Z. Ren, and S. D. Wilson, Phys. Rev. B **87**, 144405 (2013).
[21] S. Boseggia, H. C. Walker, J. Vale, R. Springell, Z. Feng, R. S. Perry, M. M. Sala, H. M. Rønnow, S. P. Collins, and D. F. McMorrow, J. Phys.: Condens. Matter **25**, 422202 (2013).
[22] B. J. Kim, H. Ohsumi, T. Komesu, S. Sakai, T. Morita, H. Takagi, and T. Arima, Science **323**, 1329 (2009).
[23] M. Ge, T. F. Qi, O. B. Korneta, D. E. De Long, P. Schlottmann, W. P. Crummett, and G. Cao, Phys. Rev. B **84**, 100402(R) (2011).
[24] C. Lu, B. Gao, H. Wang, W. Wang, S. Yuan, S. Dong, and J. Liu, Adv. Funct. Mater. **28**, 1706589 (2018).
[25] M. R. Liu, H. X. Xue, J. C. Meng, R. P. Bai, W. M. Jiang, Z. Zhang, J. Z. Ling, L. He, C. M. Xiong, R. F. Dou, and J. C. Nie, Phys. Rev. B **100**, 075129 (2019).
[26] J. Ge, D. Ma, Y. Liu, H. Wang, Y. Li, J. Luo, T. Luo, Y. Xing, J. Yan, D. Mandrus, H. Liu, X. C. Xie, and J. Wang, Nat. Sci. Rev. **7**, 1879 (2020).
[27] W. Limmer, J. Daeubler, L. Dreher, M. Glunk, W. Schoch, S. Schwaiger, and R. Sauer, Phys. Rev. B **77**, 205210 (2008).

[28] W. Y. Cui, P. Li, and H. L. Bai, J. Appl. Phys. **117**, 133904 (2015).

[29] See Supplemental Material at http://link.aps.org/supplemental/10.1103/PhysRevB.104.035301 for additional data and details on the experiments and data analysis.

[30] A. Rajapitamahuni, L. Zhang, M. A. Koten, V. R. Singh, J. D. Burton, E. Y. Tsymbal, J. E. Shield, and X. Hong, Phys. Rev. Lett. **116**, 187201 (2016).

[31] S. Boseggia, R. Springell, H. C. Walker, H. M. Ronnow, C. Rueegg, H. Okabe, M. Isobe, R. S. Perry, S. P. Collins, and D. F. McMorrow, Phys. Rev. Lett. **110**, 117207 (2013).

[32] H. Wang, C. Lu, J. Chen, Y. Liu, S. L. Yuan, S. Cheong, S. Dong, and J. Liu, Nat. Commun. **10**, 2280 (2019).

[33] Z. Ren, M. Wang, P. Liu, Q. Liu, K. Wang, G. Jakob, J. Chen, K. Meng, X. Xu, J. Miao, and Y. Jiang, Adv. Electron Mater. **6**, 2000102 (2020).

[34] A. Rajapitamahuni, L. L. Tao, Y. Hao, J. Song, X. Xu, E. Y. Tsymbal, and X. Hong, Phys. Rev. Materials **3**, 021401(R) (2019).

[35] Y. Liu, J. Yang, W. Chu, H. Du, W. Ning, L. Ling, W. Tong, Z. Qu, G. Cao, Y. Zhang, and M. Tian, Appl. Phys. Lett. **111**, 033103 (2017).

[36] A. S. Everhardt, M. DC, X. Huang, S. Sayed, T. A. Gosavi, Y. Tang, C.-C. Lin, S. Manipatruni, I. A. Young, S. Datta, J.-P. Wang, and R. Ramesh, Phys. Rev. Materials **3**, 051201(R) (2019).

[37] C. O. Avci, K. Garello, M. Gabureac, A. Ghosh, A. Fuhrer, S. F. Alvarado, and P. Gambardella, Phys. Rev. B **90**, 224427 (2014).

[38] A. Gutierrez-Llorente, L. Iglesias, B. Rodriguez-Gonzalez, and F. Rivadulla, APL Mater. **6**, 091101 (2018).

[39] B. Chen, N. Yang, N. Zhong, X. Tang, P. Yang, P. Xiang, and C. Duan, Mater. Lett. **202**, 96 (2017).